Nanoscale

PAPER

View Article Online
View Journal | View Issue

Cite this: *Nanoscale*, 2023, **15**, 7577

Silane functionalization of WS_2 nanotubes for interaction with poly(lactic acid)†

Eimear Magee,[a] Fengzai Tang,[b] Marc Walker,[c] Alla Zak,[d] Reshef Tenne[e] and Tony McNally *[a]

Functionalisation of nanofillers is required for the promotion of strong interfacial interactions with polymers and is essential as a route for the preparation of (nano)composites with superior mechanical properties. Tungsten disulphide nanotubes (WS_2 NTs) were functionalized using (3-aminopropyl) triethoxysilane (APTES) for preparation of composites with poly(lactic acid) (PLA). The WS_2 NTs : APTES ratios used were 1 : 1, 1 : 2 and 1 : 4 WS_2 NTs : APTES. The APTES formed siloxane networks bound to the NTs *via* surface oxygen and carbon moieties adsorbed on the WS_2 NTs surface, detected by X-ray photoelectron spectroscopy (XPS) studies and chemical mapping using energy dispersive X-ray spectroscopy in the scanning transmission electron microscope (STEM-EDS). The successful silane modification of the WS_2 NTs was clearly evident with both significant peak shifting by as much as 60 cm^{-1} for Si–O–Si vibrations (FTIR) and peak broadening of the A_{1g} band in the Raman spectra of the WS_2 NTs. The evolution of new bands was also observed and are associated with $Si–CH_2–CH_2$ and, symmetric and assymetric $–NH^{3+}$ deformation modes (FTIR). Further evidence for functionalization was obtained from zeta potential measurements as there was a change in surface charge from negative for pure WS_2 NTs to positive for APTES modified WS_2 NTs. Additionally, the thermal stability of APTES was shifted to much higher temperatures as it was bound to the WS_2 NTs. The APTES modified WS_2 NTs were organophilic and readily dispersed in PLA, while presence of the pendant amine and hydroxyl groups resulted in strong interfacial interactions with the polymer matrix. The inclusion of as little as 0.5 wt% WS_2 NTs modified with 2.0 wt% APTES resulted in an increase of 600% in both the elongation at break (a measure of ductility) and the tensile toughness relative to neat PLA, without impacting the stiffness or strength of the polymer.

Received 8th February 2023,
Accepted 28th March 2023

DOI: 10.1039/d3nr00583f

rsc.li/nanoscale

1. Introduction

Tungsten disulphide nanotubes (WS_2 NTs) continue to attract increased attention given their interesting and useful properties including, mechanical[1,2] (*e.g.* Young's modulus of 170 GPa and tensile strength of 16–20 GPa), and electrical and optical behaviour.[3–7] Furthermore, they have been shown to have non-toxic and biocompatible properties.[8–10] As with most 0D/1D/2D materials, there is a great interest in translating some of these properties to polymer matrices to enhance chemical and physical properties *via* effective dispersion and distribution of the NTs throughout the polymer matrix. The 1D structure of WS_2 NTs is co-centric molecular cylinders consisting of a rolled plane of W atoms sandwiched between two rolled planes of S atoms and kept together by strong covalent bonds, while the molecular S-W-S layers (cylinders) are bonded by weak van der Waals forces.[11] Weak interactions between neighbouring NTs can result in agglomeration and the formation of NT bundles. This can pose a significant technical challenge with regards to homogenous dispersion and distribution of the NTs within polymer matrices, which, if not achieved, often results in poor material properties.[12] Additionally, achieving well dispersed nanofillers relies also on the extent of interfacial interactions between the polymer matrix and the nanofiller, which is highly dependent on the surface chemistry of each material. Surface modification of inorganic nanoparticles with silane coupling agents can produce and aid dispersion and promote enhanced interfacial interactions between the nanoparticles and the polymer matrices.[12–19] Examples include (3-aminopropyl)triethoxysilane (APTES) functionalization successfully grafted *via* a hydro-

[a]*International Institute for Nanocomposites Manufacturing (IINM), University of Warwick, CV4 7AL, UK. E-mail: t.mcnally@warwick.ac.uk*
[b]*WMG, University of Warwick, CV4 7AL, UK*
[c]*Department of Physics, University of Warwick, Coventry CV4 7AL, UK*
[d]*Physics Department, Faculty of Sciences, Holon Institute of Technology - HIT, Holon 5810201, Israel*
[e]*Molecular Chemistry and Material Science, Weizmann Institute of Science, Rehovot 76100, Israel*

† Electronic supplementary information (ESI) available. See DOI: https://doi.org/10.1039/d3nr00583f

lysis mechanism on the surface of nanoparticles.[15,20–24] Silane surface functionalisation of WS_2 NTs has not been widely investigated, with a few exceptions, and limited to where the matrix is an epoxy (see however ref. 25) or for other applications. Shahar *et al.* were the first to functionalize the surface of WS_2 fullerene-like nanoparticles with organo-silane molecules and reported better dispersion in oil-based suspensions.[26] While Sade *et al.* studied the functionalisation of WS_2 NTs with both conformal humin-like coatings and APTES,[27] the authors confirmed successful attachment of APTES to the surface of the NTs. Critically, the functional amine group of APTES is then available for further interaction with polymers.

Poly(lactic acid) (PLA) is a biodegradable thermoplastic of interest in biomedical and biopolymer materials research, with applications as diverse as tissue engineering, cardiovascular implants, dental niches, drug carriers, orthopaedic engineering, cancer therapy, skin and tendon healing, and in medical tools and equipment.[28–37] However, PLA, depending on the D- and L-isomer content can have poor properties including a high degree of brittleness and low gas barrier properties.[38] Consequently, given the excellent combination of WS_2 NT mechanical and biocompatible properties, reinforcement of PLA for Bioresorbable Vascular Scaffolds (BVS)[39,40] and bone tissue engineering[41,42] are of great interest. WS_2 NTs have already been shown to readily dispersible in PLA and at loadings as low as 0.5 wt% increase the elastic modulus, yield strength and strain-at-failure of the polymer by 20%, 23% and 35%, respectively.[43] This behaviour is attributed to effective NT dispersion and the nucleating effect the NTs have on the PLA which in turn has a significant effect on PLA crystalline content.[44–48] Interestingly, in another study, inclusion of these NTs was reported to have had a plasticising effect on the polymer.[40]

In this paper, we report for the first time the functionalisation of WS_2 NTs with APTES and their use as a functional filler for PLA. The effectiveness of the silane grafting to the surface of NTs is investigated as an approach to enhance NT dispersion in the polymer matrix and promote strong interfacial interaction between the WS_2 NTs and PLA as a route for improving the mechanical properties of PLA.

2. Experimental

2.1 Materials

Details of the synthesis and characterization of the WS_2 NTs is described in ref. 49. Briefly, the NTs were synthesized *via* vapor–gas–solid (VGS) high-temperature reaction between tungsten oxide and reactive gases, such as hydrogen sulfide and hydrogen, using nitrogen as carrier gas, custom made quartz reactor with specially designed porous reaction cell and one-zone horizontal split furnace.[49] Poly(L-lactic acid) (PLA) was supplied by Corbion Luminy® LX17 consisting of at least 96% L-isomer. (3-Aminopropyl)triethoxysilane (APTES, 98%) and Dichloromethane (DCM, 99.8%) were purchased from Sigma Aldrich and used as received.

2.2 Preparation of APTES modified WS_2 NTs

0.25 g of WS_2 NTs were dispersed in 30 ml dichloromethane (DCM) by ultrasonic bath treatment (3 minutes). The APTES was added to this solution in ratios of 1 : 1 (0.25 g WS_2 : 0.2643 ml APTES), 1 : 2 (0.25 g WS_2 : 0.5285 ml APTES) and 1 : 4 (0.25 g WS_2 : 1.057 ml APTES), the density of APTES is 0.946 g ml^{-1}. The APTES : WS_2 NTs DCM solutions were then mechanically stirred at 500 rpm overnight at room temperature. The silane modified WS_2 NTs were dried at room temperature (RT) for 8 hours followed by drying at 40 °C under vacuum for 12 hours.

2.3 Preparation of composites of APTES : WS_2 NTs and PLA

Composites of APTES modified WS_2 NTs were prepared *via* solution mixing and solvent casting. Firstly, 0.5 wt% WS_2 NTs (0.05 g) were fully dispersed in 30 ml of DCM assisted using ultrasonic bath treatment (3 min) and then 0.5, 1.0 and 2.0 wt% APTES (0.05 g/0.0526 ml, 0.1 g/0.1057 ml, 0.2 g/0.211 ml respectively, for different NTs:APTES ratios) was added, followed by stirring overnight to allow the completion of the reaction. Second, PLA (10 g) was dissolved in 50 mL of DCM under magnetic stirring in a 250 mL round-bottom flask at RT. Once prepared, APTES : WS_2 NTs DCM solutions were added to the PLA–DCM solution and mechanically stirred overnight at 500 rpm. The resulting solutions were cast in Petri dishes and dried at RT for 8 h followed by drying at 40 °C under vacuum for 12 h to produce composites of PLA with APTES modified WS_2 NTs in a film form. These films were then hot pressed using a Collin Hot Press (P 200 PM) at 190 °C in a mould for 4 min and cooled to RT at a rate of 10 K min^{-1} to obtain the final film with a thickness of ~0.5 mm.

2.4 Characterisation

Fourier transform infrared (FTIR) spectra were collected in transmission mode using a Bruker Tensor 27 FTIR spectrometer. Measurements were recorded in the wavenumber range 500 cm^{-1}–4000 cm^{-1} with a resolution of 2 cm^{-1} and 16 scans were accumulated.

Thermogravimetric analysis (TGA) was carried out using a Mettler Toledo instrument, using alumina pans, in the temperature range 25 °C to 1000 °C at a heating rate of 10 K min^{-1} under a nitrogen atmosphere.

X-ray photoelectron spectroscopy (XPS) measurements were carried out using a Kratos Axis Ultra DLD spectrometer (Kratos Analytical, Manchester, UK). Samples were mounted on electrically conductive carbon tape upon the sample bar and loaded into the spectrometer. Once a pressure better than 1×10^{-6} mbar had been reached, the samples were transferred to the main analysis chamber. The samples were illuminated by a mono-chromated Al Kα X-ray source ($h\nu$ = 1486.7 eV) and flooded with low energy electrons from a charge neutraliser in order to prevent the surface from becoming positively charged during the experiment. Data were collected at a take-off angle of 90° in a hemispherical analyser using a pass energy of 160 eV for survey spectra and 20 eV for high resolution core level spectra (resolution approx. 0.4 eV). Data were analysed by the CasaXPS software package, using mixed Gaussian–Lorentzian

(Voigt) line-shapes and Shirley backgrounds. The spectrometer was calibrated with the Ag $3d_{5/2}$ peak and Fermi edge of clean polycrystalline Ag prior to the start of the experiments, with the transmission function determined by various clean metallic foils. The binding energy scale was calibrated during the analysis, with the C–C/C–H component in the C 1s region at 285.0 eV as the reference point.

The Raman spectra of neat WS_2 NTs and APTES functionalised NTs were collected on a Renishaw Invia spectrometer fitted with a 633 nm laser. They were recorded under ambient conditions with a 50× magnification objective using 5% of laser power (0.5 mW) spot focused on the sample with an exposure time of 10 seconds and up to 1600 accumulations.

Scanning electron microscopy (SEM) images were obtained on a Zeiss Sigma field emmission instrument using an operating voltage of 3 kV. WS_2 NTs and APTES modified WS_2 NTs were carefully deposited onto double-sided conductive carbon adhesive tape on an SEM stub. The composites of APTES functionalised WS_2 NTs and PLA were cryo-fractured and also placed on adhesive carbon tape and the fractured surfaces examined. All samples were sputter coated with a ~20 nm thick film of carbon using a Safematic CCU-010 Compact Coating Unit. Scanning Transmission Electron Microscopy (STEM) imaging of the NTs was carried out using a FEI (Thermo Fisher Scientific) Talos F200X microscope, operating at 200 kV throughout the analysis. The microscope had a X-FEG (Field Emission Gun) high-brightness electron source and was fitted with a Super-X EDS (Energy Dispersive X-ray Spectroscopy) system with integrated four silicon drift detectors, providing a solid angle of 0.9 srad for rapid chemical composition mapping. Samples were prepared by dispersion in methanol and transferred on to holy carbon coated grids. The data were acquired using either FEI TIA™ or Velox™ software, and both High-Angle Annular Dark-Field (HAADF) images and Bright-Field (BF) images were taken simultaneously.

Zeta potential measurements were conducted on all samples diluted with 0.5 ml methanol and vigorously shaken to ensure good dispersion before being loaded into an Omega zeta potential cuvette. Samples were run in triplicate for 100 runs at 25 °C.

Tensile mechanical testing was performed using an Instron 5800R instrument operating Bluehill 2 software. 5–7 dog bone shaped specimens were prepared and tested for each composite. Tests were carried out with a video extesometer using a constant crosshead speed of 1 mm min^{-1}.

DSC measurements were carried out using a Mettler Toledo DSC 1 under a nitrogen atmosphere, a heating rate of 10 K min^{-1} from 25 to 200 °C, isotherm at 200 °C for 2 minutes and cooled at 10 K min^{-1} from 200 to 25 °C. The percentage crystallinity (X_c) of the samples was calculated using the following eqn (1):

$$\left(\frac{\Delta H_m - \Delta H_{cc}}{\omega \Delta H_m^\circ}\right) \times 100 \quad (1)$$

where, ΔH_m, ΔH_{cc} are the enthalpy of melting and cold crystallisation, respectively, ω is the weight fraction of PLA in each composite, and ΔH_m° is the melting enthalpy of a theoretically 100% crystalline PLA which has been reported to be 93.7 J g^{-1}.[50]

3. Results and discussion

To determine if APTES functionalisation of the NTs was successful, the FTIR spectra of WS_2 NTs : APTES in the ratios 1 : 1, 1 : 2 and 1 : 4 in comparison with the spectra for WS_2 NTs and APTES alone were recorded (Fig. 1). The FTIR spectrum of WS_2 NTs does not display any peaks in the infrared due to the WS_2 having no dipole moment as a result of its symmetry modification which causes a change in polarizability.[51] A consequence of being rolled into 1D multiwalled nanotubes is a loss of symmetry and the WS_2 becomes an asymmetrical crystal. This results in WS_2 NTs having new properties, including displaying a bulk photovoltaic effect, piezoelectricity and ferroelectricity.[49,52,53] APTES displays characteristic peaks at 3383 cm^{-1} and 2974 cm^{-1} which are related to amine NH_2 stretching. Peaks at 1604 cm^{-1} and 1483 cm^{-1} and related peaks are assigned to NH_2 deformation bending modes of amine groups, which are strongly bonded in the hydrogen to the silanol groups to form cyclic structures.[54] Peaks at 1442 cm^{-1} and 1390 cm^{-1} correlate to O–H bending, while those at 1294 cm^{-1} and 1165 cm^{-1} are associated with C–O stretching of the aromatic ester. Asymmetric and symmetric Si–O–Si vibrations were recorded at 1073 cm^{-1} and 765 cm^{-1}, as well as a Si–O–C asymmetric peak at 1100 cm^{-1}.[55] Si–OH stretching and bending vibrations are observed at 954 cm^{-1} and 853 cm^{-1}, respectively.[56] The peak at 677 cm^{-1} is associated with N–H bending.

For the APTES functionalized WS_2 NTs at all ratios (Fig. 1(b)), similar FTIR transmittance spectra were obtained, and with increasing silane content the intensity of all peaks increases monotonically, suggesting successful grafting of the silane moiety to the NT surface. The spectra for APTES modified WS_2 NTs shows a shift of the N–H stretching vibrations with respect to neat APTES from 3383 cm^{-1} and 2974 cm^{-1} to 3348 cm^{-1} and 3270 cm^{-1}, which are superimposed on a broad peak in the 3500–2500 cm^{-1} region associated with O–H stretching mode as a result of water absorption in the sample. However, the evolution of new bands is identified and depicted in Fig. 1(c), the one at 1570 cm^{-1} is assigned to the asymmetric $-NH_3^+$ deformation mode, with the corresponding symmetric $-NH_3^+$ mode at 1470 cm^{-1}.[21] The band at 1305 cm^{-1} is characteristic of C–N stretching in amines, while $Si–CH_2–R$ vibrational modes are typically observed in the range 1250–1200 cm^{-1},[57] therefore the band at 1232 cm^{-1} is associated with $Si–CH_2–CH_2$. An O–H band is observed again for the functionalized NTs but is shifted to 1383 cm^{-1}. For APTES modified WS_2 NTs, there is a shift of all peaks in the region 1150–600 cm^{-1} (Fig. 1(d)) relative to pure APTES. The symmetric Si–O–Si vibrations are red-shifted by 61 cm^{-1} from 1073 cm^{-1} (APTES) to 1012 cm^{-1} when grafted on to WS_2 NTs in the ratio of 1 : 1. A further shift of 7 cm^{-1} to 1005 cm^{-1} is observed for the WS_2 NTs : APTES 1 : 2 sample, and again a

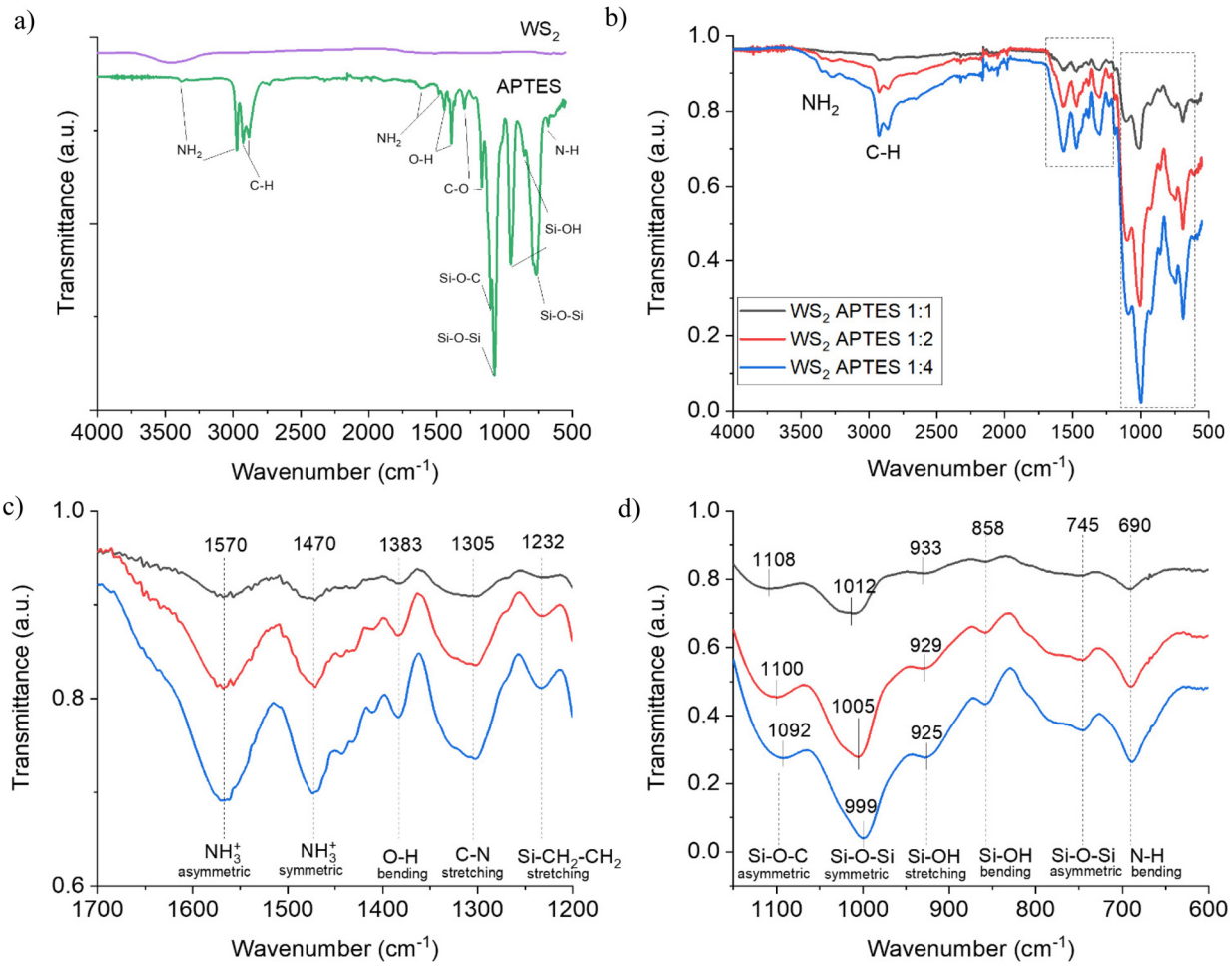

Fig. 1 FTIR transmittance spectra of, (a) WS_2 NTs and APTES, (b) APTES functionalized WS_2 NTs in ratios of 1 : 1, 1 : 2 and 1 : 4, (c) spectra enlarged in the range 1700–1200 cm^{-1} and (d) in the range 1150–600 cm^{-1}.

shift of a further 7 cm^{-1} to 998 cm^{-1} for WS_2 NTs : APTES 1 : 4. The asymmetric Si–O–Si vibration band is observed at the lower (realative to the symmetirc Si–O–Si vibration) wavenumber of 745 cm^{-1} irrespective of the ratio of WS_2 NTs to APTES. There was also a variation in the peak shift of band position for the asymmetric Si–O–C from 1100 cm^{-1} for APTES to 1108 cm^{-1}, 1100 cm^{-1} and 1092 cm^{-1} for 1 : 1, 1 : 2, 1 : 4 WS_2 NTs : APTES, respectively. Si–OH stretching and bending vibrations are observed at 929 cm^{-1}, 858 cm^{-1} and 780 cm^{-1}, respectively.[56] Furthermore, the N–H bending peak blue shifts by 13 cm^{-1} to 690 cm^{-1} after the surface modification of the WS_2 NTs. These new bands, observed for APTES modified WS_2 NTs in comparison to APTES alone and shifting of the peaks with increased ratio of APTES, provides evidence for the formation of a siloxane network on the surface of the WS_2 NTs, confirming strong interaction of APTES with the surface of the NTs.

The effectiveness of surface functionalization of the WS_2 NTs with APTES was also investigated by studying the thermal stability of the surface modified NTs using thermogravimetric analysis under N_2 atmosphere, Fig. 2. The onset of thermal degradation of APTES alone (even under a non-oxidative atmosphere) was just above ambient temperaure with a 90% mass loss by 200 °C. In contrast, the WS_2 NTs are shown to be thermally stable across the whole temperature range (25 °C–1000 °C) examined with a total weight loss of just 2.5%. When bound to the WS_2 NTs the thermal decomposition profile of APTES is shifted to higher temperatures with weight losses of 32.1%, 32.9% and 36.4%, for WS_2 NT : APTES in the ratios 1 : 1, 1 : 2 and 1 : 4, respectively. This increase in mass loss with increasing APTES concentration further supports the idea that the APTES is bound to the WS_2 NTs. Additionally, the DTG curves for the APTES modified WS_2 NTs (Fig. 2(b)) show that, irrespective of the APTES concentration the weight loss occurs in three main stages. Below 100 °C, mass loss is attributed to the removal of water from the surface of the NTs. A second small peak with maxima at ~329 °C for the 1 : 1 and 1 : 2 sample, increasing to 354 °C for the 1 : 4 sample, is associated possibly with the removal of residual surfactant. Above 400 °C a third peak with maxima at 500 °C is observed perhaps derived from the decomposition of the functional groups chemically anchored to the surface of NTs given the

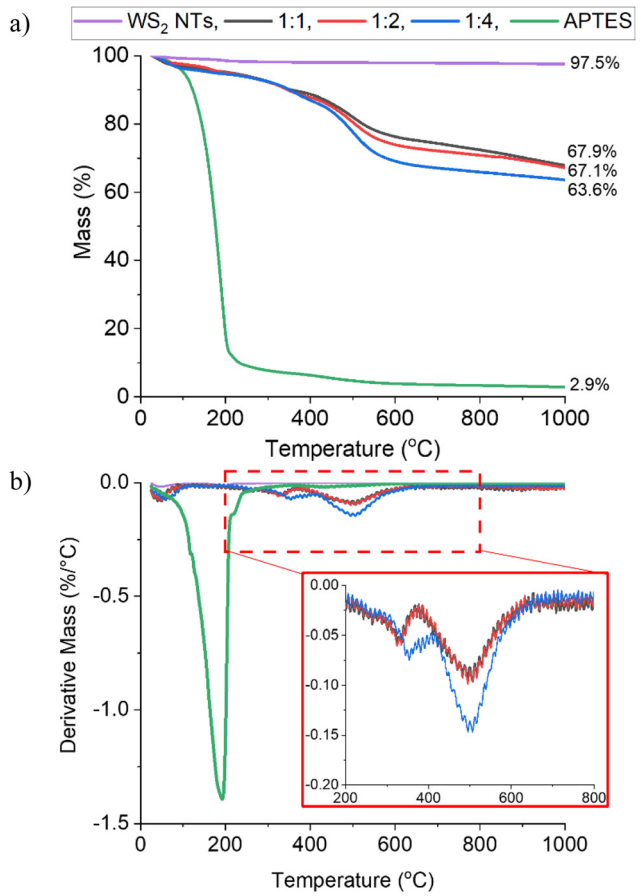

Fig. 2 (a) TGA weight loss curves and (b) DTA curves for WS_2 NTs, APTES and APTES modified WS_2 NTs at different ratios.

increased grafting of APTES at a ratio of 1 : 4 (WS_2 NT : APTES) and the formation of a siloxane network. The extent of the grafting was estimated from further analysis of the TGA data.[58] After mass normalization, the number of grafted chains were calculated using eqn (2):

$$\text{Chain}_{\text{graft}} = \frac{W_{\text{loss}}\%}{(100 - W_{\text{loss}}\%) \times M_{\text{w}_{\text{molecule}}}} \times N_{\text{a}} \quad (2)$$

where, $W_{\text{loss}}\%$ represents the percentage weight loss (from TGA) in the temperature range 200 °C and 800 °C, $M_{\text{w}_{\text{molecule}}}$ is the molecular weight of the grafted molecule of APTES (221.37 g mol^{-1}), and N_{a} is Avogadro's number (6.02214076 × 10^{23}). This temperature range was chosen assuming residual APTES was removed below 200 °C. Knowing the specific surface area (SSA_{BET}) of the WS_2 NTs,[59] from BET measurements = 19.19 $\text{m}^2\ \text{g}^{-1}$ the coverage density (σ) can be readily calculated using eqn (3) and the values are listed in Table 1:

$$\sigma = \frac{\text{Chain}_{\text{graft}}}{\text{SSA}_{\text{BET}}} \quad (3)$$

The grafting density (σ) increases with increasing APTES concentration rendering the NTs more organophilic.

Table 1 Grafting density APTES on the surface of WS_2 NTs in air

	$W_{\text{loss}}\%$ (200–800 °C)	$\text{Chain}_{\text{graft}}$ (mol g^{-1})	σ (mol nm^{-2})
WS_2 APTES 1 : 1	22.55	7.92×10^{20}	41.3
WS_2 APTES 1 : 2	28.41	1.08×10^{21}	56.3
WS_2 APTES 1 : 4	35.14	1.47×10^{21}	76.8

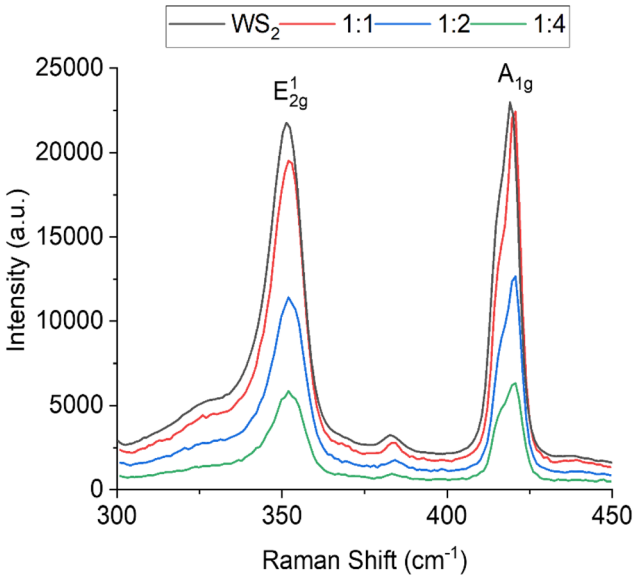

Fig. 3 Raman spectra of WS_2 NTs and APTES modifed WS_2 NTs.

The Raman spectrumof WS_2 NTs displays peaks characteristic to WS_2 at 351.1 cm^{-1} and 419.0 cm^{-1}, these are the most prominent Raman modes found in the spectra and are associated with the in-plane vibrations (E_{2g}) of chalcogen atoms and out-of-plane vibrations (A_{1g}) of chalcogen and transition metal atoms, respectively (Fig. 3).[60] After functionalization with APTES, a slight blueshift of both peaks, the $E_{2g}{}^1$ to 352.2 cm^{-1} and the A_{1g} to 420.7 cm^{-1} is observed for all APTES concentrations. This shift in peak position is representative of molecular absorption on the surface of the nanotubes.[61] The A_{1g} peak can be seen to split and the FWHM (full width at half maximum) increases with increasing APTES concentration ($\Delta\text{FWHM} \approx 1.4\ \text{cm}^{-1}$ from neat WS_2 NTs to WS_2 : APTES 1 : 4). Note that the splitting of the A_{1g} is attributed to the lower symmetry of the nanotube compared to the bulk, which induces a new peak B_{1u} at 416 cm^{-1}.[62] The changes in the shape of the A_{1g} peak is evidence for covalent functionalization due to the presence of functional groups attached to the chalcogen atoms on the surface of the sulphur atom of the WS_2 NTs.[63] The covalent bonding of the APTES to the outermost sulfur leads to loss of symmetry enhancing the B_{1u} Raman peak, which is a silent mode in bulk WS_2. It should be noted that not only the addition of functional groups but also the structure (curvature) of the NTs can activate the B_{1u} mode. Additionally, with increasing APTES concentration, the intensity of the peaks

Table 2 Element atomic % extrapolated from deconvoluted XPS data for WS_2 NTs and APTES functionalized WS_2 NTs

Sample	C	O	S	W	N	Si
WS_2 NTs	19.97	7.25	49.26	23.51	—	—
WS_2 APTES 1 : 1	48.72	23.93	1.34	0.7	11.17	14.13
WS_2 APTES 1 : 2	60.98	22.83	1.21	0.64	5.61	8.73
WS_2 APTES 1 : 4	55.6	23.18	0.89	0.38	8.03	11.92

decreases, perhaps as a consequence of the APTES coating (siloxane network) on the surface of the NTs. These changes in the Raman spectra strongly support molecular physisorption of APTES on the surface of the WS_2 NTs.

To further determine if APTES functionalization of the WS_2 NT surface was successful, XPS spectra were recorded for all samples (deconvoluted curves are displayed in the ESI, see Fig. S1†) and the relevant atomic percentages are listed in Table 2. The atomic percentages are in agreement with our pre-

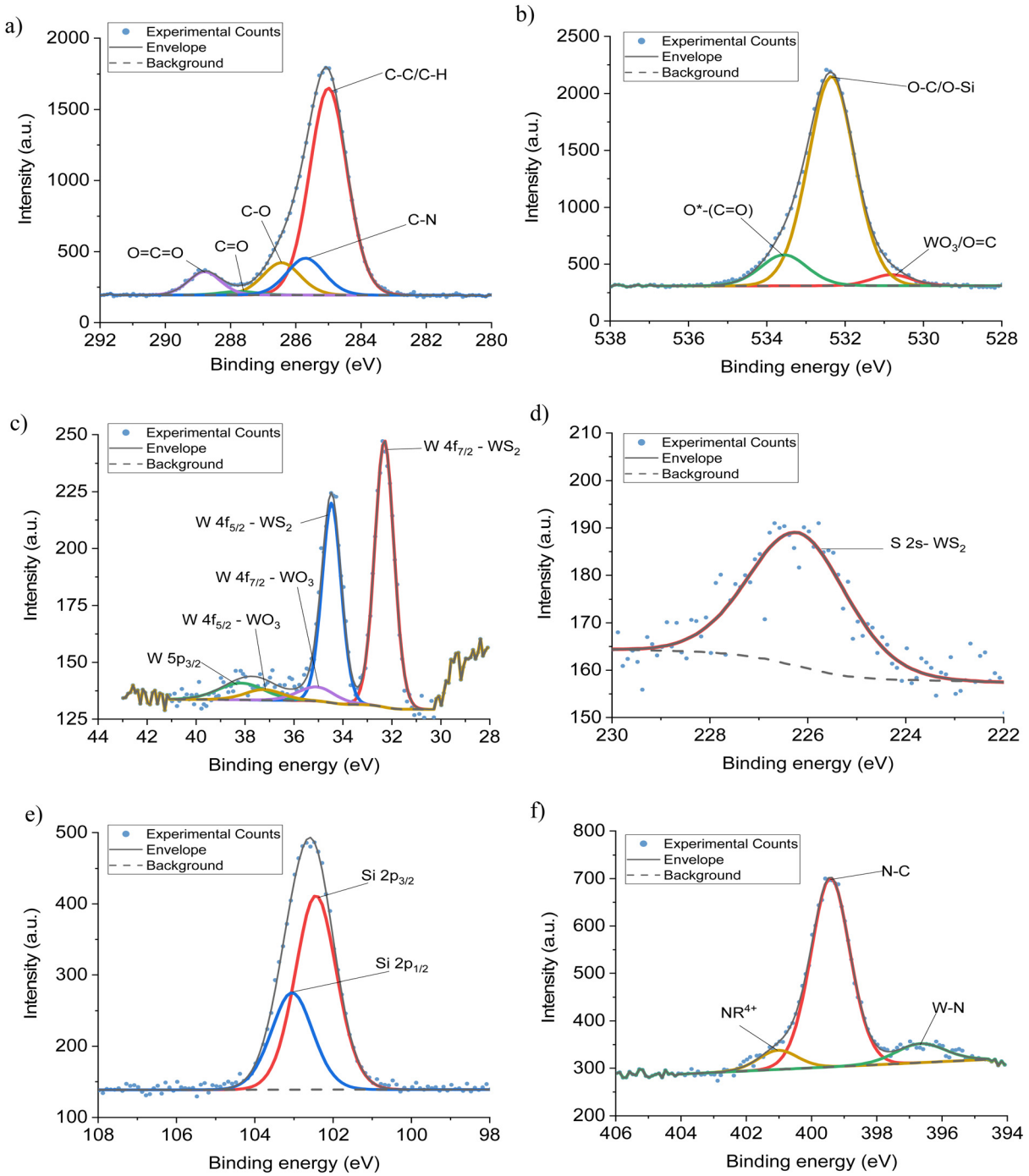

Fig. 4 Deconvoluted XPS spectra, (a) C 1s, (b) O 1s, (c) W 4f, (d) S 2s, (e) Si 2p (f) N 1s regions from the XPS spectra of WS_2–APTES at a ratio of 1 : 4.

vious studies[64] confirming successful grafting of silane through carbon and oxygen. Both are loosely attached to the surface of the NTs due to atmospheric conditions, while Si and N are also detected for the WS_2 NTs : APTES samples. Increased atomic % for C and O (Table 2) in comparison to WS_2 NTs is ascribed to the successful attachment of APTES to the WS_2 NTs.

Fig. 4 shows representative decovoluted spectra for the APTES functionalised WS_2 NTs. The remainder of the XPS data are presented in the ESI Fig. S2–S5 and Tables S2–S5.† Deconvoluted peaks in the C 1s region (Fig. 4(a)), display a similar chemical composition consisting of five components: C–C/C–H, C–N, C–O, C═O, O═C–O. The addition of APTES on the surface of WS_2 NTs is identified with the evolution of a new peak at 285.7 eV from C–N bonding, characteristic of silane functionalisation of other NTs.[25] From the O 1s region (Fig. 4(b)) peaks derived from WO_3/O═C, O–C/O–Si and O* (C═O) were recorded. After functionalization with APTES, the evolution of another new peak at 532.35 eV was observed, corresponding to O–Si/O–C bonding. The O–C peak due to atmospheric contamination was present prior to the addition of the APTES. The increase in peak intensity relative to the other components suggests O–Si bonding, which overlaps with

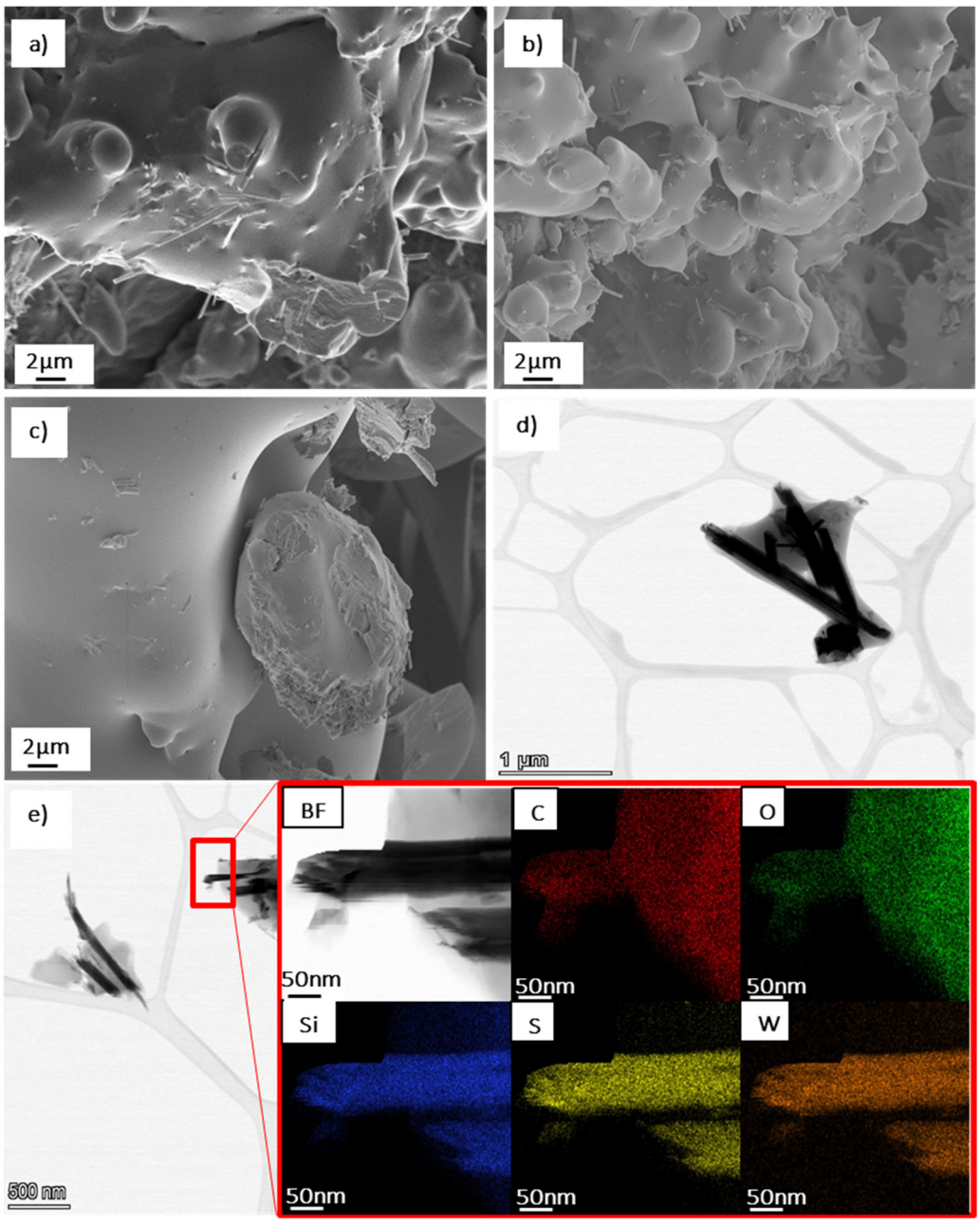

Fig. 5 SEM and STEM imaging of APTES functionalised WS_2 NTs. (a–c) SEM images of WS_2 NTs : APTES at 1 : 1, 1 : 2 and 1 : 4, respectively. (d) STEM of WS_2 NTs : APTES at 1 : 4, and (e) STEM and EDS mapping of the WS_2NTs–APTES 1 : 4 sample.

O–C in binding energy. An increase of approximately 12% in the area under the oxygen peak confirms binding of the APTES to oxygen, which is attached to the surface of the WS_2 NTs. The presence of different Si environments (Fig. 4(e)) is confirmed from deconvoluted Si $2p_{3/2}$ and Si $2p_{1/2}$ data which correlates with Si–O–C or Si–O–Si in the two energy states, again further affirming grafting of APTES to surface molecules on the WS_2 NTs. For the N 1s region (Fig. 4(f)) deconvoluted peaks corresponding to N–C, NR^{4+} and evidence of W–N bonding for the WS_2 NTs : APTES 1 : 4 sample were obtained. The N–C bonding in characteristic of APTES, showing it is successfully attached to the surface of the NTs.[65] NR^{4+} bonding is suggestive of an amine reaction between APTES with molecules on the surface of the WS_2 NTs, however this cannot be confirmed with these XPS spectra. Additionally, the observed W–N bonding confirms successful functionalization of APTES to the WS_2 NTs, while it also suggests that by increasing the ratio of APTES to WS_2 NTs the grafting density of silane on the NT surface can be increased. For APTES functionalised WS_2 NTs, it should be noted that it is likely that the plasmon loss features from Si 2s photoemission overlap with the S 2p photoemission, possibly leading to incorrect identification of chemical environments and/or elemental composition. Therefore, for these samples, the S 2s region (Fig. 4(d)) was examined, however there is no indication of APTES interaction with sulphur atoms in this region.

SEM and STEM imaging were carried out to examine the NTs morphology after functionalisation with APTES, see Fig. 5. The WS_2 NTs were well dispersed in the APTES silane network, forming a cohesive continuous morphoogy at all ratios, see SEM images (Fig. 5(a)–(c)). This further supports strong interfacial interaction between the silane and the surface of the NTs. The aspect ratio of the NTs were also examined with NT lengths up to 6 μm measured, and a small portion of significantly shortened NTs (see STEM image in Fig. 5(d)), with lengths as small as 0.64 μm observed, most likley due to the sonication process during sample preparation.[3] We reported the structure and morphology of the WS_2 NTs in great detail in our previous work.[64] From high resolution STEM images, (Fig. 5(d) and (e)), the APTES is seen to clearly coat the surface of the WS_2 NTs, an observation confirmed from EDS mapping. Tungsten (W) and sulphur (S) can be clearly identified for the NTs structure, while silicon (Si) from APTES is strongly attached to the surface of the NTs and is also surrounding the NTs. EDS analysis indicates also that carbon (C) and oxygen (O) (from the APTES) are found on the NT surface.

To confirm further the attachment of APTES to the surface of the WS_2 NTs, the zeta (ζ) potential of the WS_2 NTs and APTES modified NTs with increasing APTES concentration were measured in methanol dispersions. WS_2 NTs alone (1 : 0) have a charge of −26.7 ± 0.71 mV, due to the sulphur atoms exposed on the surface of the NTs.[66] After reaction with APTES, the ζ potential values gradually become increasingly

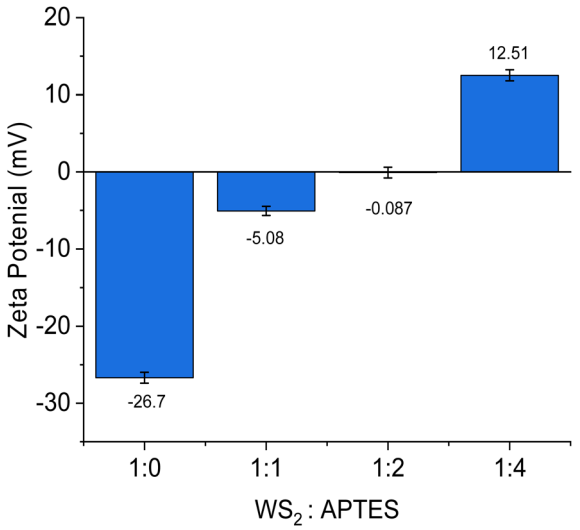

Fig. 6 ζ potential for WS_2 NTs, and change in ζ for APTES–WS_2 NTs with increasing APTES content.

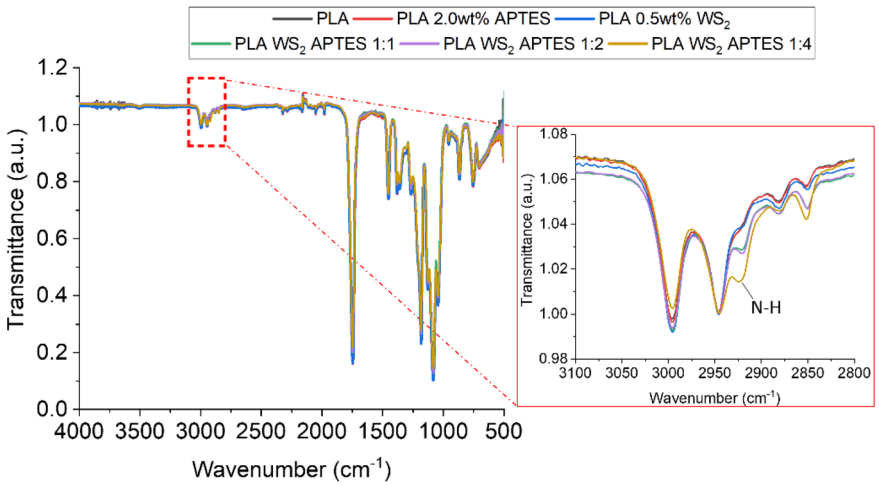

Fig. 7 FTIR spertra of for PLA, a blend of PLA and APTES composites of PLA with APTES modified WS_2 NTs.

positive with increasing APTES concentration, Fig. 6. The concentration of APTES is critical to the extent of functionalization and APTES grafted to the surface of the WS_2 NTs. The change in ζ potential is derived from the presence of amine groups (from APTES) on the NT surface, as amine groups are protonated to positively charged ammonium producing a higher ζ potential value.[65,67] This observation is a qualitative indication of successful functionalization of WS_2 NTs with APTES. The reaction between PLA and APTES follows a condensation and grafting mechanism that results in the formation of a N–H bond.[68] Consequently, there is the evolution of a band associated with N–H stretching at 2921 cm^{-1} in the FTIR spectra that becomes more intense and shifts by 4 cm^{-1} to 2925 cm^{-1} with increasing APTES content, see Fig. 7.

The rationale for functionalising WS_2 NTs with APTES is to provide a route to aid effective dispersion of the NTs in polymers and to promote strong interfacial interactions between both, such that some bulk properties of the polymer can be improved. To examine this hypothesis, APTES modified WS_2 NTs were dispersed in PLA and solvent cast to produce films and specimens for tensile mechanical testing.

The representative optical photographs shown in Fig. 8(a), compare film samples for neat PLA, composites of PLA and WS_2 NTs, and composites of PLA and APTES modified WS_2

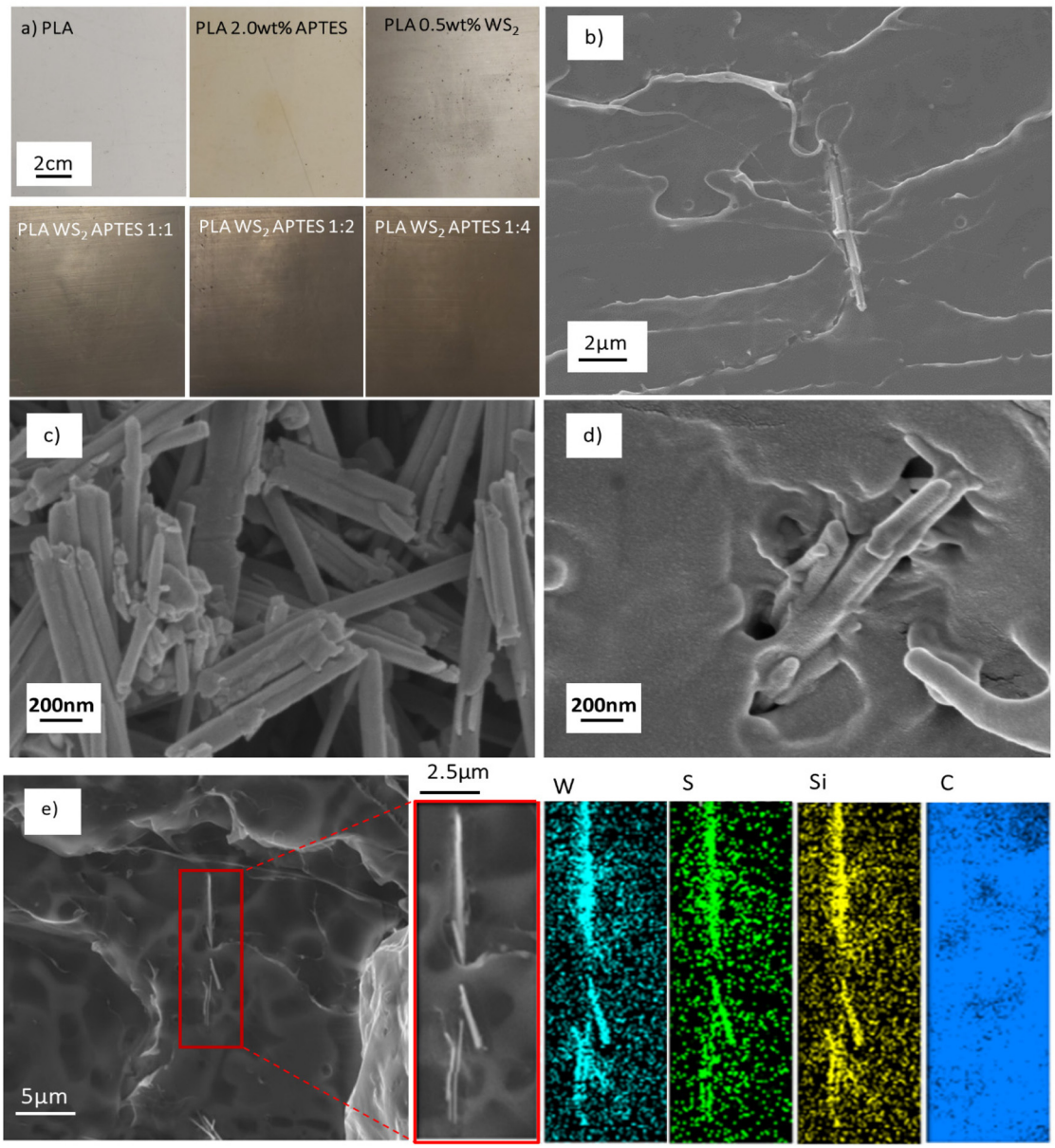

Fig. 8 (a) Representative optical photographs of film samples of PLA alone and corresponding composites and SEM micrographs of (b) composite of PLA and APTES modified WS_2 NTs (1 : 4), (c) unmodified WS_2 NTs, (d) composite of PLA and WS_2 NTs : APTES 1 : 4 at higher magnification and (e) composite of PLA WS_2 NTs : APTES 1 : 4 with corresponding EDS of highlighted area.

NTs. In agreement with previous studies, the WS_2 NTs disperse very well within the PLA matrix.[43,48,69,70] Nevertheless, APTES functionalised WS_2 NTs are much more uniformly dispersed as clearly seen from these images suggesting increased surface interaction and compatibility between APTES modified WS_2 NTs and the PLA matrix. Extensive SEM imaging of the composites of PLA and APTES modified WS_2 NTs (Fig. 8(b) and (c)) across the length scales did not show NT agglomerations and individual NTs were observed (Fig. 8(b)), supporting uniform dispersion of the NTs in the PLA matrix. Additionally, SEM-EDS was used for surface elemental analysis of these composites, Fig. 8(e). This analysis clearly identifies tungsten and sulphur from the NTs, while also confirming the presence of silicon from APTES only on the surface of NTs, in agreement with the EDS analysis reported in Fig. 5. (The detected carbon on the entire analysed area stems from the carbon coating of the sample.) This observation is further verification of silane functionalisation of the WS_2 NTs.

To assess the effectiveness of silane modification of the WS_2 NTs on the mechanical properties of PLA, tensile tests of neat PLA, blends of PLA and APTES as control samples and, composites of PLA and APTES modified WS_2 NTs were measured. Representative stress–strain curves for all the specimens are shown in Fig. 9. The Young's modulus (MPa), maximum tensile stress (MPa), elongation at break (%) and the tensile toughness (kJ m^{-3}) as a function of the ratio of WS_2 NTs : APTES were determined and the values are listed in Tables 3 and 4. For the blends of PLA and APTES only, *i.e.* with no WS_2 NTs added, neat PLA had an elongation at break of ~33% with stress oscillation observed beyond necking.[71] Upon addition of 2 wt% APTES to PLA, an initial decrease in tensile properties is observed before an increase to values approaching that of the PLA alone (Table 3). The mechanical properties with 1.0 wt% APTES loading exhibit reduced performance compared to neat PLA, which may be associated with aminolysis causing scission of the polymer chains and the material becomes brittle.[68,72] However, at 2 wt% APTES the mechanical properties are similar to that of neat PLA. This suggests that at 2.0 wt% APTES there is strong interfacial interactions with the polymer chains and the microstructure of PLA is not degraded when mixed with APTES. The inclusion of 0.5 wt% unfunctionalised WS_2 NTs resulted in a degradation of mechanical properties, ~15% reduction in Young's modulus relative to neat PLA, indicative of poor interfacial interaction between the WS_2 NTs and the PLA matrix,[73] resulting in a reduction in PLA ductility and toughness. In contrast, inclusion of APTES functionalized WS_2 NTs to the same PLA resulted in a systematic increase in the tensile mechanical properties with increasing WS_2 NTs : APTES ratio, Fig. 9(b). When the ratio of WS_2 NTs : APTES was 1 : 4 there was a enhancement in mechanical properties, including an almost 600% increase in elongation at break and tensile toughness from 0.99 kJ m^{-3} to 6.88 kJ m^{-3} (Table 4). Critically, there was little change in the maximum tensile strength and Young's modulus of PLA, irrespective of the WS_2 NT : APTES ratio. The significant increase in elongation at break and toughness on addition of APTES modified

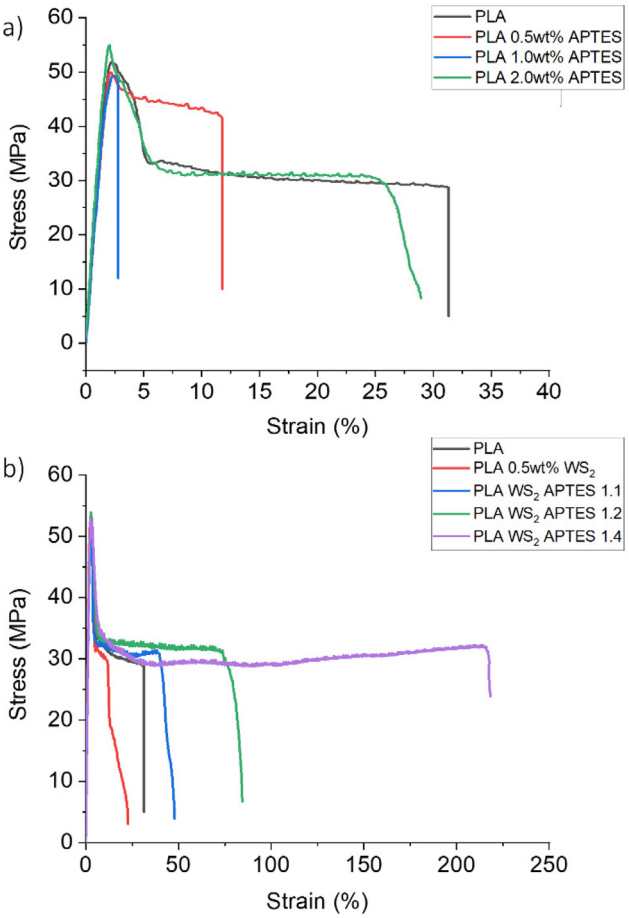

Fig. 9 Representative stress–strain curves for neat PLA relative to those for (a) blends of PLA and APTES and (b) composites of PLA and APTES modified WS_2 NTs.

Table 3 Tensile mechanical properties of PLA and blends of PLA and APTES

Sample	Modulus (MPa)	Maximum tensile stress (MPa)	Elongation at break (%)	Tensile toughness (kJ m^{-3})
PLA	3414 ± 178	57 ± 4	33 ± 4	1.0 ± 0.10
PLA 0.5 wt% APTES	3085± 114	50 ± 4	17 ± 3	0.4 ± 0.05
PLA 1.0 wt% APTES	2883 ± 73	49 ± 2.5	3.3 ± 0.3	0.1 ± 0.02
PLA 2.0 wt% APTES	3439 ± 72	54 ± 3	31 ± 2.5	0.9 ± 0.03

Table 4 Tensile mechanical properties of PLA and composites of PLA APTES modified WS_2 NTs

Sample	Modulus (MPa)	Maximum tensile stress (MPa)	Elongation at break (%)	Tensile toughness (kJ m^{-3})
PLA	3414 ± 178	57 ± 4	33 ± 4	1.0 ± 0.10
PLA 0.5 wt% WS_2	2922 ± 148	54 ± 4	23 ± 2	0.6 ± 0.08
PLA WS_2 APTES 1 : 1	3222 ± 179	52 ± 3	51 ± 6	1.5 ± 0.25
PLA WS_2 APTES 1 : 2	3493 ± 102	53 ± 1	84 ± 14	2.6 ± 0.40
PLA WS_2 APTES 1 : 4	3323 ± 151	55 ± 2	208 ± 18	6.9 ± 0.41

WS_2 NTs is a consequence of the improved and very strong interfacial interactions between the NTs and polymer and the role APTES is playing in aiding the dispersion of WS_2 NTs in the PLA matrix. The interaction *via* the amine and hydroxyl groups of APTES bound to the NTs and PLA provides a route for effective stress transfer at the interface from the polymer to the filler.

Given the fact that many nanomaterials can nucleate polymers and alter the crystallization behaviour of the matrix, the thermal properties of the composites were studied by DSC. DSC curves (cooling and melting curves) for unfilled PLA, blends of PLA and APTES, composites of PLA and unmodified WS_2 NTs and composites of PLA and APTES modified WS_2 NTs were recorded, see Fig. 10.

The T_g of neat PLA was determined to be 54 °C and it remained constant on the addition of APTES or WS_2 NTs (Table 5). However, on addition of APTES modified WS_2 NTs, the T_g of PLA increased by 2 °C, although this is likley to be within instrument error. Given the fact that the change in T_g was minor, as was the case with the Young's modulus and tensile strength of PLA on inclusion of silane functionalised WS_2 NTs, the change in the mechanical properties are not due to a plasticizing effect or major change in the PLA crystalline content.[74]

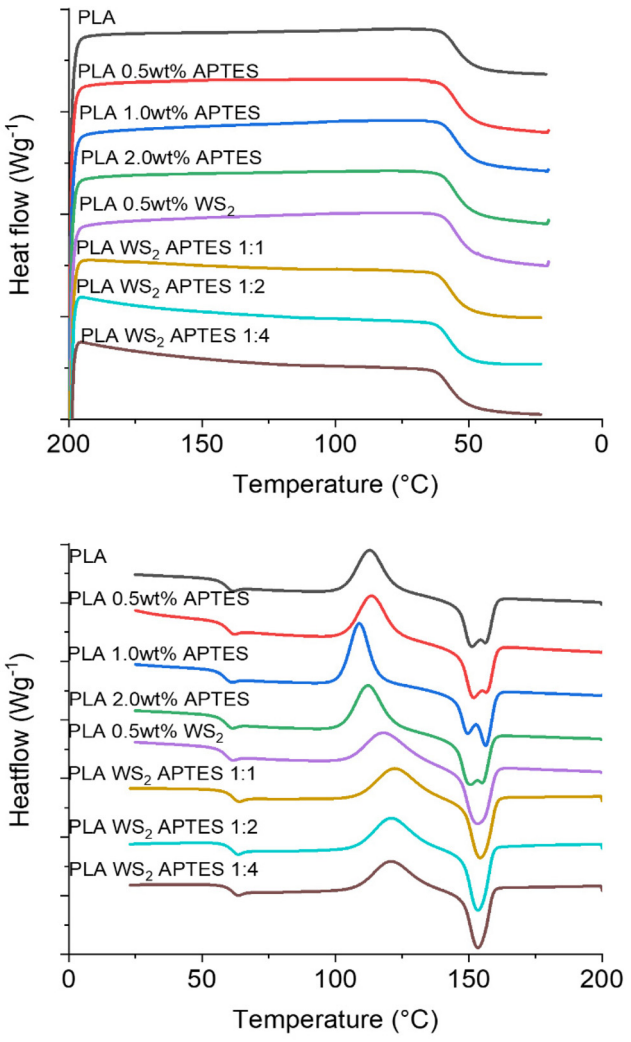

Fig. 10 DSC thermograms for PLA and its blends with APTES and composites with APTES modified WS_2 NTs showing (a) first cooling cycle and (b) second heating cycle.

Table 5 DSC parameters for neat PLA, blends of PLA and APTES, and composites of PLA and APTES modified WS_2 NTs

Sample	T_g (°C)	T_{cc} (°C)	ΔH_{cc}	T_{m1} (°C)	T_{m2} (°C)	ΔH_m	X_c (%)
PLA	54	113	25	151	156	27	1.7
PLA/0.5 wt% APTES	54	113	25	151	156	27	2.7
PLA/1.0 wt% APTES	53	109	28	150	156	29	0.9
PLA/2.0 wt% APTES	54	112	27	153	155	29	2.1
PLA/0.5 wt% WS_2	54	118	24	153	—	28	4.2
PLA WS_2 APTES 1 : 1	56	122	24	154	—	28	3.6
PLA WS_2 APTES 1 : 2	56	121	25	153	—	27	2.5
PLA WS_2 APTES 1 : 4	56	121	23	153	—	25	2.5

Moreover, the PLA used in this study was highly amorphous (at least 96% L-isomer) and the minor crystalline component very slow to crystallise, such that no crystalline peak is observed in the cooling curve (Fig. 10(a)). However, a significant broad cold crystallisation peak is observed in the heating cycle (Fig. 10(b)) for all the samples. The neat PLA has a broad T_{cc} peak centred at 113 °C, while the incorporation of WS_2 NTs shifted the T_{cc} by 5 °C to 118 °C. The NTs have a strong nucleating effect on the PLA, but a limited effect on the overall crystalline content (X_c = 4.2%) due to the high L-isomer content. There is a further shift of 3 °C in T_{cc} to 121 °C upon inclusion of the APTES modified WS_2 NTs. This further shift, some 8 °C higher than that for unfilled PLA is a consequence of the better WS_2 NT dispersion and increased NT surface area available as nucleating sites for the polymer, but again the high L-isomer content hinders crystallite growth. A doublet of melting peaks were observed for the neat PLA and blends of PLA and APTES with T_{m1} at 151 ± 1 °C and T_{m2} at 155–156 °C. Both peaks are characteristic of PLA and can be attributed to the melting–recrystallization–melting processes of PLA lamellae. The first peak is ascribed to the melting of new lamellae formed during the heating cycle (*i.e.* T_{cc}), the second peak is the melting–recrystallisation of primary thin lamellae at relatively higher temperature.[75] Interestingly, the DSC curves for the composites of APTES modified WS_2 NTs and PLA exhibit a single melting peak at 152 °C, which is attributed to the highly dispersed modified NTs promoting nucleation and PLA crystal growth. However, due to slow crystallisation kinetics of the PLA used in this study, the composites remain almost fully amorphous with a crystalline content remaining below 5%. Therefore, the significant enhancement in the ductility and toughness of the PLA on inclusion of APTES modified WS_2 NTs must be derived from the high level of dispersion and strong interfacial interactions between the APTES coated NTs and the polymer matrix and not because of changes in the PLA microstructure.

4. Conclusions

(3-Aminopropyl) triethoxysilane (APTES) was sucessfully grafted to the surface of WS_2 NTs, the greater the concentration of APTES used the greater the extent of its binding to the NT surface. Extensive characterisation of the APTES functionalised WS_2 NTs using a combination of spectroscopy (FTIR, Raman, XPS), thermal-gravimetric analysis (TGA), electron microscopy (SEM-EDS, STEM-EDS) and Zeta potenial measurements confirmed a high level of grafting of the APTES through the formation of siloxane networks on the NT surface. Additionally, the APTES was covalently bonded owing to the presence of functional groups attached to the surface sulfur atoms of the WS_2 NTs. APTES modification of the WS_2 NT surface significantly improved the extent of WS_2 NT dispersion in the PLA matrix and promoted strong interfacial interactions between the NTs and the polymer. This resulted in a significant increase in the elongation at break, by 600%, and the tensile toughness of PLA from 1.0 kJ m^{-3} to 6.8 kJ m^{-3} (~600%) on inclusion of WS_2 NTs : APTES (1 : 4). This work highlights for the first time the effectiveness of silane functionalization of 1D WS_2 nanotubes as a route to forming strong interfacial interactions between inorganic nanoparticles and polymers to produce composites with significantly enhanced ductility and toughness without sacrificing stiffness and strength, properties useful for food packaging or biomedical applications. Specifically, given the excellent combination of increased tensile strength and toughness obtained in this work, combined with the known radio-opacity and non-toxicity of WS_2 NTs and, the biocompatibility of PLA, reinforcement of PLA with WS NTs may find application as Bioresorbable Vascular Scaffolds (BVS).

Conflicts of interest

There are no conflicts to declare.

Acknowledgements

The authors thank WMG, University of Warwick and the "Weizmann UK-Making Connections" program for funding this work. RT acknowledges the support of the Estate of Manfred Hecht and the Estate of Diane Recanati and is also grateful to the Perlman Family Foundation and the Kimmel Center for Nanoscale Science.

References

1 K.-A. Ifat, *et al.*, On the Mechanical Behavior of WS2 Nanotubes under Axial Tension and Compression, *Proc. Natl. Acad. Sci. U. S. A.*, 2006, (3), 523.
2 I. Kaplan-Ashiri, *et al.*, Mechanical behavior of individual WS2 nanotubes, *J. Mater. Res.*, 2004, **19**(2), 454–459.
3 H. Rennhofer and B. Zanghellini, Dispersion State and Damage of Carbon Nanotubes and Carbon Nanofibers by Ultrasonic Dispersion: A Review, *Nanomaterials*, 2021, **11**(6), 1469.
4 C. Zhang, *et al.*, High-performance photodetectors for visible and near-infrared lights based on individual WS2 nanotubes, *Appl. Phys. Lett.*, 2012, **100**(24), 243101.
5 Y. J. Zhang, *et al.*, Optoelectronic response of a WS 2 tubular p–n junction, *2D Mater.*, 2018, **5**(3), 035002.
6 A. Grillo, *et al.*, WS2 Nanotubes: Electrical Conduction and Field Emission Under Electron Irradiation and Mechanical Stress, *Small*, 2020, **16**(35), 2002880.
7 T. V. Shubina, *et al.*, Excitonic emission in van der Waals nanotubes of transition metal dichalcogenides, *Ann. Phys.*, 2019, **531**(6), 1800415.
8 M. Pardo, *et al.*, Low Cytotoxicity of Inorganic Nanotubes and Fullerene-Like Nanostructures in Human Bronchial Epithelial Cells: Relation to Inflammatory Gene Induction and Antioxidant Response, *Environ. Sci. Technol.*, 2014, **48**(6), 3457–3466.
9 E. B. Goldman, *et al.*, Biocompatibility of tungsten disulfide inorganic nanotubes and fullerene-like nanoparticles with salivary gland cells, *Tissue Eng., Part A*, 2015, **21**(5–6), 1013–1023.
10 R. Tenne, Recent advances in the research of inorganic nanotubes and fullerene-like nanoparticles, *Front. Phys.*, 2013, **9**(3), 370–377.
11 R. Tenne and L. Margulis, Polyhedral and cylindrical structures of tungsten disulphide, *Nature*, 1992, **360**(6403), 444.
12 Y. Ding, Y. Chen and J. Zheng, Dispersion of nanoparticles in polymer matrices with well-designed ligands as dispersant/emulsifier/comonomer, *Compos. Sci. Technol.*, 2018, **156**, 215–222.
13 S. Kango, *et al.*, Surface modification of inorganic nanoparticles for development of organic–inorganic nanocomposites—A review, *Prog. Polym. Sci.*, 2013, **38**(8), 1232–1261.
14 L. M. Hamming, *et al.*, Effects of dispersion and interfacial modification on the macroscale properties of TiO(2) polymer matrix nanocomposites, *Compos. Sci. Technol.*, 2009, **69**(11–12), 1880–1886.
15 Y. Liu, *et al.*, APTES Modification of Molybdenum Disulfide to Improve the Corrosion Resistance of Waterborne Epoxy Coating, *Coatings*, 2021, **11**, 178.
16 K.-J. Kim and J. L. White, Silica surface modification using different aliphatic chain length silane coupling agents and their effects on silica agglomerate size and processability, *Compos. Interfaces*, 2002, **9**(6), 541–556.
17 E. Ukaji, *et al.*, The effect of surface modification with silane coupling agent on suppressing the photo-catalytic activity of fine TiO2 particles as inorganic UV filter, *Appl. Surf. Sci.*, 2007, **254**(2), 563–569.
18 M. Sabzi, *et al.*, Surface modification of TiO2 nano-particles with silane coupling agent and investigation of its effect on the properties of polyurethane composite coating, *Prog. Org. Coat.*, 2009, **65**(2), 222–228.

19 E. Tang, *et al.*, Fabrication of zinc oxide/poly(styrene) grafted nanocomposite latex and its dispersion, *Eur. Polym. J.*, 2007, **43**(10), 4210–4218.
20 A. Zarinwall, *et al.*, Comprehensive Characterization of APTES Surface Modifications of Hydrous Boehmite Nanoparticles, *Langmuir*, 2021, **37**(1), 171–179.
21 D. Meroni, *et al.*, A Close Look at the Structure of the TiO2-APTES Interface in Hybrid Nanomaterials and Its Degradation Pathway: An Experimental and Theoretical Study, *J. Phys. Chem. C*, 2017, **121**(1), 430–440.
22 Y. Wang, *et al.*, Enhanced quantum efficiency from a mosaic of two dimensional MoS2 formed onto aminosilane functionalised substrates, *Nanoscale*, 2016, **8**(24), 12258–12266.
23 S. Ryu, K. Kim and J. Kim, Silane surface treatment of boron nitride to improve the thermal conductivity of polyethylene naphthalate requiring high temperature molding, *Polym. Compos.*, 2018, **39**, E1692–E1700.
24 A. Miranda, L. Martínez and P. A. A. De Beule, Facile synthesis of an aminopropylsilane layer on Si/SiO_2 substrates using ethanol as APTES solvent, *MethodsX*, 2020, **7**, 100931.
25 M. Shneider, *et al.*, Nanoinduced morphology and enhanced properties of epoxy containing tungsten disulfide nanoparticles, *Polym. Eng. Sci.*, 2013, **53**(12), 2624–2632.
26 C. Shahar, *et al.*, Surface functionalization of WS2 fullerene-like nanoparticles, *Langmuir*, 2010, **26**(6), 4409–4414.
27 H. Sade, *et al.*, Testing of WS2 Nanoparticles Functionalized by a Humin-Like Shell as Lubricant Additives, *Lubricants*, 2018, **6**(1), 3.
28 V. DeStefano, S. Khan and A. Tabada, Applications of PLA in modern medicine, *Eng. Regener.*, 2020, **1**, 76–87.
29 I. Armentano, *et al.*, Multifunctional nanostructured PLA materials for packaging and tissue engineering, *Prog. Polym. Sci.*, 2013, **38**(10), 1720–1747.
30 I. G. Athanasoulia, *et al.*, Study of thermomechanical, structural and antibacterial properties of poly(lactic acid) reinforced with graphene oxide nanoparticles via melt mixing, *Polym. Int.*, 2020, 995–1007.
31 W. J. Choi, *et al.*, Rapid development of dual porous poly(lactic acid) foam using fused deposition modeling (FDM) 3D printing for medical scaffold application, *Mater. Sci. Eng. C*, 2020, **110**, 110693.
32 R. E. Elsayed, T. M. Madkour and R. A. Azzam, Tailored-design of electrospun nanofiber cellulose acetate/poly (lactic acid) dressing mats loaded with a newly synthesized sulfonamide analog exhibiting superior wound healing, *Int. J. Biol. Macromol.*, 2020, 1984–1999.
33 C. Han, *et al.*, Enhanced drug delivery, mechanical properties and antimicrobial activities in poly(lactic acid) nanofiber with mesoporous Fe3O4-COOH nanoparticles, *Colloids Surf., A*, 2018, **559**(20), 104–114.
34 C. Hu, *et al.*, Bioinspired surface modification of orthopedic implants for bone tissue engineering, *Biomaterials*, 2019, **219**, 119366.
35 R. A. Ilyas, *et al.*, *Chapter 6 - Nanocellulose/Starch Biopolymer Nanocomposites: Processing, Manufacturing, and Applications*, in *Advanced Processing, Properties, and Applications of Starch and Other Bio-Based Polymers*, ed. F. M. Al-Oqla and S. M. Sapuan, Elsevier, 2020, pp. 65–88.
36 N. Ploypetchara, *et al.*, Blend of Polypropylene/Poly(lactic acid) for Medical Packaging Application: Physicochemical, Thermal, Mechanical, and Barrier Properties, *Energy Procedia*, 2014, **56**, 201–210.
37 M. Santoro, *et al.*, Poly(lactic acid) nanofibrous scaffolds for tissue engineering, *Adv. Drug Delivery Rev.*, 2016, **107**, 206–212.
38 R. M. Rasal, A. V. Janorkar and D. E. Hirt, Poly(lactic acid) modifications, *Prog. Polym. Sci.*, 2010, **35**(3), 338–356.
39 K. Ramachandran, *et al.*, Crimping-induced structural gradients explain the lasting strength of poly L-lactide bioresorbable vascular scaffolds during hydrolysis, *Proc. Natl. Acad. Sci. U. S. A.*, 2018, **115**(41), 10239–10244.
40 L. Rocher, *et al.*, Interaction of Poly L-Lactide and Tungsten Disulfide Nanotubes Studied by In Situ X-ray Scattering during Expansion of PLLA/WS2NT Nanocomposite Tubes, *Polymer*, 2021, **13**(11), 1764–1783.
41 G. Lalwani, *et al.*, Tungsten disulfide nanotubes reinforced biodegradable polymers for bone tissue engineering, *Acta Biomater.*, 2013, **9**(9), 8365–8373.
42 W. Wang, *et al.*, Polymer Composites Reinforced by Nanotubes as Scaffolds for Tissue Engineering, *Int. J. Polym. Sci.*, 2014, **2014**, 805634.
43 H. Shalom, *et al.*, Strong, tough and bio-degradable polymer-based 3D-ink for fused filament fabrication (FFF) using WS2 nanotubes, *Sci. Rep.*, 2020, **10**(1), 1–8.
44 H. Shalom, *et al.*, Nanocomposite of Poly(l-Lactic Acid) with Inorganic Nanotubes of WS2, *Lubricants*, 2019, **7**(3), 28.
45 A. M. Díez-Pascual and M. Naffakh, Mechanical and thermal behaviour of isotactic polypropylene reinforced with inorganic fullerene-like WS2 nanoparticles: Effect of filler loading and temperature, *Mater. Chem. Phys.*, 2013, **141**(2), 979–989.
46 M. Naffakh and M. D.-P. Ana, Thermoplastic Polymer Nanocomposites Based on Inorganic Fullerene-like Nanoparticles and Inorganic Nanotubes, *Inorganics*, 2014, (2), 291.
47 M. Naffakh, *et al.*, Opportunities and challenges in the use of inorganic fullerene-like nanoparticles to produce advanced polymer nanocomposites, *Prog. Polym. Sci.*, 2013, **38**(8), 1163–1231.
48 M. Naffakh and C. Marco, Isothermal crystallization kinetics and melting behavior of poly(l-lactic acid)/WS2 inorganic nanotube nanocomposites, *J. Mater. Sci.*, 2015, **50**(18), 6066–6074.
49 P. Chithaiah, *et al.*, Solving the "MoS2 Nanotubes" Synthetic Enigma and Elucidating the Route for Their Catalyst-Free and Scalable Production, *ACS Nano*, 2020, **14**(3), 3004–3016.
50 S. Jia, *et al.*, Morphology, crystallization and thermal behaviors of PLA-based composites: Wonderful effects of hybrid

GO/PEG via dynamic impregnating, *Polymer*, 2017, **9**(10), 528.

51 Y. S. S. Leung, Novel biopolymer constructs: physical properties and antimicrobial efficacy, in *Warwick Manufacturing Group*, University of Warwick, 2018.

52 Y. Zhang, *et al.*, Enhanced intrinsic photovoltaic effect in tungsten disulfide nanotubes, *Nature*, 2019, **570**(7761), 349–353.

53 Y. Sun, *et al.*, Mesoscopic sliding ferroelectricity enabled photovoltaic random access memory for material-level artificial vision system, *Nat. Commun.*, 2022, **13**(1), 1–8.

54 N. Majoul, S. Aouida and B. Bessaïs, Progress of porous silicon APTES-functionalization by FTIR investigations, *Appl. Surf. Sci.*, 2015, **331**, 388–391.

55 T. Jiang, *et al.*, Enhanced mechanical properties of silanized silica nanoparticle attached graphene oxide/epoxy composites, *Compos. Sci. Technol.*, 2013, **79**, 115–125.

56 S. Z. Haeri, M. Asghari and B. Ramezanzadeh, Enhancement of the mechanical properties of an epoxy composite through inclusion of graphene oxide nanosheets functionalized with silica nanoparticles through one and two steps sol-gel routes, *Prog. Org. Coat.*, 2017, **111**, 1–12.

57 A. S. Maria Chong and X. S. Zhao, Functionalization of SBA-15 with APTES and Characterization of Functionalized Materials, *J. Phys. Chem. B*, 2003, **107**(46), 12650–12657.

58 D. Selli, *et al.*, Optimizing pegylation of TiO2 nanocrystals through a combined experimental and computational study, *Chem. Mater.*, 2019, **31**(18), 7531–7546.

59 S. Wei, *et al.*, Improved Electrochemical Performance of NTs-WS2@ C Nanocomposites for Lithium-Ion and Sodium-Ion Batteries, *ACS Appl. Mater. Interfaces*, 2022, **14**(41), 46386–46400.

60 A. Berkdemir, *et al.*, Identification of individual and few layers of WS2 using Raman Spectroscopy, *Sci. Rep.*, 2013, **3**(1), 1–8.

61 S. Bertolazzi, *et al.*, Molecular chemistry approaches for tuning the properties of two-dimensional transition metal dichalcogenides, *Chem. Soc. Rev.*, 2018, **47**(17), 6845–6888.

62 M. Staiger, *et al.*, Excitonic resonances in WS_2 nanotubes, *Phys. Rev. B: Condens. Matter Mater. Phys.*, 2012, **86**(16), 165423.

63 D. Voiry, *et al.*, Covalent functionalization of monolayered transition metal dichalcogenides by phase engineering, *Nat. Chem.*, 2015, **7**(1), 45–49.

64 E. Magee, *et al.*, WS2 Nanotubes as a 1D Functional Filler for Melt Mixing with Poly(lactic acid): Implications for Composites Manufacture, *ACS Appl. Nano Mater.*, 2022, **5**(5), 6385–6397.

65 H. Sade and J. P. Lellouche, Functionalization of Tungsten Disulfide Nanotubes with a Conformal Humin–Like Shell, *Adv. Mater. Interfaces*, 2016, **3**(20), 1600307.

66 E. Chibowski and A. Waksmundzki, A relationship between the zeta potential and surface free energy changes of the sulfur/n-heptane—water system, *J. Colloid Interface Sci.*, 1978, **66**(2), 213–219.

67 W. Talavera-Pech, *et al.*, Effects of different amounts of APTES on physicochemical and structural properties of amino-functionalized MCM-41-MSNs, *J. Sol-Gel Sci. Technol.*, 2016, **80**(3), 697–708.

68 X. Meng, *et al.*, Supertough PLA-Silane Nanohybrids by in Situ Condensation and Grafting, *ACS Sustainable Chem. Eng.*, 2018, **6**(1), 1289–1298.

69 M. Naffakh, C. Marco and G. Ellis, Development of novel melt-processable biopolymer nanocomposites based on poly(L-lactic acid) and WS2 inorganic nanotubes, *CrystEngComm*, 2014, **16**(23), 5062–5072.

70 L. Tammaro, *et al.*, Effect of tungsten disulfide (WS2) nanotubes on structural, morphological and mechanical properties of poly(L-lactide) (PLLA) films, in *9th International Conference on "Times of Polymers And Composites"*, American Institute of Physics.

71 C. Wan, *et al.*, Stress-oscillation behaviour of semi-crystalline polymers: the case of poly(butylene succinate), *Soft Matter*, 2018, **14**(45), 9175–9184.

72 Y. Lu, *et al.*, Improved mechanical properties of polylactide nanocomposites-reinforced with cellulose nanofibrils through interfacial engineering via amine-functionalization, *Carbohydr. Polym.*, 2015, **131**, 208–217.

73 D. Metın, *et al.*, The effect of interfacial interactions on the mechanical properties of polypropylene/natural zeolite composites, *Composites, Part A*, 2004, **35**(1), 23–32.

74 H. Lim and S. W. Hoag, Plasticizer effects on physical-mechanical properties of solvent cast Soluplus® films, *AAPS PharmSciTech*, 2013, **14**(3), 903–910.

75 M. Naffakh, *et al.*, The Effect of WS2 Nanosheets on the Non-Isothermal Cold- and Melt-Crystallization Kinetics of Poly(l-lactic acid) Nanocomposites, *Polymer*, 2021, **13**(13), 2214.

